ADVANCED FUNCTIONAL MATERIALS
www.afm-journal.de

Autonomous Sensing Architected Materials

*Mattia Utzeri, Hülya Cebeci, and Shanmugam Kumar**

Integrating autonomous sensing materials into future applications necessitates developing advanced multiscale multiphysics predictive models. This study introduces an experimentally informed predictive framework for autonomous sensing architected materials, combining theoretical and computational methodologies. By incorporating stress-dependent electrical resistivity through anisotropic piezoresistive constitutive effects, alongside considering material, geometric, and contact nonlinearities, the proposed multiscale model captures the architecture-dependent piezoresistive responses of lattice composites produced via additive manufacturing of polyetherimide (PEI)/carbon nanotube (CNT) nanoengineered feedstock. The PEI/CNT composite exhibits exceptional strength (105 MPa), stiffness (3368 MPa), and strain sensitivity (gauge factor ≈13), translating into remarkable piezoresistive characteristics for the PEI/CNT lattice composites, surpassing existing works (gauge factor ≈3 to 11). This multiscale finite element model accurately predicts both macroscopic piezoresistive responses and the influence of architectural and topological variations on electric current paths, validated via infrared thermography analysis. Additionally, an Ashby chart for the gauge factor of PEI/CNT lattice composites suggests their prediction through a scaling law similar to mechanical properties, underscoring the tunable strain and damage sensitivity of these materials. The combined experimental, theoretical, and numerical findings offer critical insights into optimizing piezoresistive composites through architected design, with profound implications for smart orthopedics, structural health monitoring, sensors, batteries, and other multifunctional applications.

1. Introduction

The advent of composite materials that seamlessly integrate structural and functional properties has marked a significant advancement in the realm of multifunctional materials. These materials exhibit the capability to perceive and respond to diverse external stimuli such as thermal,[1] electrical,[2] magnetic,[3] and optical inputs.[4,5] Among them, piezoresistive composites stand out for their unique ability to convert mechanical stress or strain into electrical resistance signals, thereby enabling real-time monitoring of environmental conditions and the detection of internal damages crucial for assessing material/structural integrity.[6,7] Applications of these materials span a wide spectrum, from innovative components like wearable sensors,[2,8] smart medical devices,[9,10] prosthetics with real perceptions,[11] to autonomous sensing structures.[12] In recent years, additive manufacturing (AM) has played a pivotal role in advancing piezoresistive composites by facilitating the creation of intricate geometries and architectures.[13,14] This capability enhances their multifunctional prowess while preserving superior weight-specific mechanical properties.[15–17]

Numerous studies have explored the autonomous sensing capabilities of these materials, evaluating piezoresistive performances through experiments that tailor electrical properties by manipulating the type, weight fraction, and distribution of conductive fillers[18–20] within the matrix material.[21] However, the proliferation of autonomous sensing composites must keep pace with the development of coupled multiphysics predictive models spanning micro- to macro-scales to ensure their seamless integration into future innovative applications, thereby bridging the gap between material research and practical implementation. Against this backdrop, this study aims to develop a predictive framework through a multiscale piezoresistive finite element (FE) modeling approach coupled with a robust material characterization strategy. This combined approach seeks to guide the design and optimization of piezoresistive lattice composites tailored for advanced autonomous sensing applications. The efficacy of this predictive framework is evaluated through a real-case scenario focusing on the piezoresistive behavior of additively manufactured architected composites composed of polyetherimide (PEI) infused with 3 wt.% Carbon nanotubes (CNT) using the

M. Utzeri, S. Kumar
Sustainable Multifunctional Materials and Additive Manufacturing (SM²AM) Laboratory
James Watt School of Engineering
University of Glasgow
Glasgow G12 8QQ, UK
E-mail: msv.kumar@glasgow.ac.uk
M. Utzeri
Department of Industrial Engineering and Mathematical Sciences
Polytechnic University of Marche
Ancona 60121, Italy
H. Cebeci
Faculty of Aeronautics and Astronautics
Istanbul Technical University
Istanbul 34469, Turkey

The ORCID identification number(s) for the author(s) of this article can be found under https://doi.org/10.1002/adfm.202411975

DOI: 10.1002/adfm.202411975

Fused Filament Fabrication (FFF) technique, which represents a unique contribution to the literature.

Traditionally, predicting the piezoresistive properties of composites has centered on the microstructural scale due to the random arrangement of conductive fillers within the matrix. The inherent randomness significantly impacts the electrical resistivity of the material, influenced by percolation thresholds, filler interactions, and the stress state.[22,23] While various micromechanics-based analytical and numerical approaches exist to estimate the electrical resistivity of bulk composites based on these factors,[24,25] modeling the piezoresistive behavior of lattice composites necessitates a multiscale approach. This is because the electrical resistivity of lattice composites is intricately dependent on the resistivity of the bulk composite (microscale), the unit cell topology (mesoscale), and the complex stress distribution in 3D space induced by lattice deformation (macroscale). Recent advancements have described this link through the introduction of the fourth-rank piezoresistivity tensor. Π_{ijlk},[25,26] which connects mechanical strain or stress to fractional changes in electrical resistivity. However, existing studies predominantly focus on numerical validation of bulk composite responses under uniaxial testing conditions, highlighting the computational challenges associated with multiscale multiphysics FE analysis for lattice composites or real components/structures. These challenges hinder the complete integration of mechanical and piezoresistive nonlinearities (including constitutive, geometrical, and contact nonlinearities) and the interaction between macroscale architectural features and local mechanical/electrical characteristics, which are essential for monitoring the structural health of materials/structures. Thus, developing a comprehensive predictive piezoresistive FE model requires overcoming these computational hurdles.

Subsequently, the suitability of the FE model must be evaluated from both mechanical and multiphysics perspectives, given its departure from purely mechanical considerations. The effectiveness of the FE piezoresistive model should encompass comparisons between mechanical behaviors and piezoresistive characteristics, spanning from macroscale lattice composites' stress-strain responses to the delineation of local electric current paths in ligaments governing the architectural influence on piezoresistive responses. Moreover, ensuring the robustness of the FE model warrants a precise piezoresistive material characterization strategy that accounts for mechanical interactions with the evolution of electrical resistance, a facet under-documented in piezoresistive materials literature. It is crucial to note that while electrical resistance serves as the measured extrinsic property, the piezoresistive phenomenon is intrinsically affected by both geometrical changes (alterations in composite dimensions) and constitutive effects (modifications in electrical resistivity).

This study aims to comprehensively address these gaps by providing an engineering-oriented framework for predicting the piezoresistive response of lattice composites. The framework includes a material characterization strategy, a multiscale multiphysics-based FE model formulation, and complete multiscale validation of both electrical and mechanical attributes. Following an analytical description, the piezoresistive material characterization strategy integrates traditional mechanical testing across multiple directions, such as compression, tensile, and Charles-Smith tests, akin to those used for piezoelectric materials.[27,28] The investigation into the piezoresistive response of PEI/CNT bulk composites involves the calibration of a piezoresistive model based on a cubic symmetric piezoresistive tensor and a concrete damage plasticity model. Subsequently, piezoresistive responses of additively manufactured PEI/CNT lattice composites are explored through experimental assessments and FE analyses, incorporating stress-dependent electrical resistivity in 3D using subroutines and external coding within the Abaqus environment. The FE model is validated by comparing experimentally measured macroscale stress-strain and piezoresistive responses of architected PEI/CNT lattice composites. Additionally, the experimental electric current paths within these composites are verified through thermographic analysis. This comprehensive examination of piezoresistive effects, underpinned by novel numerical insights, enhances understanding of optimizing structural and multifunctional properties through geometric design across various scales.

2. Piezoresistive Modeling of Composites

Piezoresistive composite, commonly utilized in electronics for "active sensors"[5] and as smart materials with autonomous sensing capabilities for structural applications, exhibits variations in electrical resistance, R, when subjected to external stimuli such as mechanical stress, σ, and/or temperature. In tensorial notation, the resistance tensor, R_{ij}, can be written as

$$R_{ij} = \rho_{ij} \left(\sigma_{ij}, T\right) \frac{L_k}{A_k} \tag{1}$$

where ρ_{ij} is the electrical resistivity tensor of the piezoresistive material, influenced by the stress tensor σ_{ij} and temperature T, encapsulating the material properties. The length-to-area tensor, $\frac{L_k}{A_k}$, represents the geometry of the electrically conducting material. Thus, the piezoresistive response of materials encompasses both geometrical effects and changes in electrical resistivity due to the material's anisotropy and/or alterations in microstructure. The electric conduction law defines the relationship between the electric field Φ and the electric current density J, through electrical resistivity, given by:

$$\Phi_i = \rho_{ij} \left(\sigma_{ij}, T\right) J_j \tag{2}$$

where Φ_i is the electric field within the material and J_j is the electric current density flowing through it. The electrical resistance can be derived from Equation (2), assuming. Φ_i and J_j are time-independent (i.e., under steady-state electric conductions) while applying Φ_i within the conductor and using the second Ohm's law. It's worth noting that piezoresistive materials do not inherently generate an electrical potential when deformed, unlike piezoelectric materials, which produce an electric potential difference in response to external mechanical stimuli.[5] The following sections delve into the piezoresistive behavior of parent and architected lattice materials.

2.1. Piezoresistive Modeling of Elastoplastic Composites

In an unstrained state, the electrical resistivity tensor ρ_{ij}, of homogeneous piezoresistive material is diagonal, with diagonal terms

defined by the electrical resistivity in the unstrained state ρ_0. Upon being subjected to mechanical deformation, the electrical resistivity accordingly changes. The evolution of tensor ρ_{ij} can generally be expressed as:

$$\rho_{ij} = \rho_0 \left(\delta_{ij} + \frac{\Delta\rho_{ij}(\sigma_{ij})}{\rho_0} \right) \tag{3}$$

where δ_{ij} is the Kronecker delta. The relationship between the fractional change in the components of the electrical resistivity tensor ($\frac{\Delta\rho_{ij}}{\rho_0}$) and mechanical strain or stress is established through the fourth-order piezoresistivity tensor Π_{ijlk}, as described below:[27]

$$\frac{\Delta\rho_{ij}}{\rho_0} = \Pi_{ijlk}\sigma_{ij} \tag{4}$$

Depending on how the loading influences the electrical resistivity along different directions, Π_{ijlk} may assume various forms, thus demonstrating symmetries and special cases akin to those observed in the elasticity tensor such as isotropy, and orthotropy.[29] Composites such as CNT-filled polymers[25] or CNT-incorporated smart concrete[26] demonstrate cubic crystal symmetry, leading to the tensor Π_{ijlk} assuming the following form:

$$\Pi_{ijkl} = \Pi_{11}\ \delta_{ij}\delta_{kl} + \Pi_{12}\left(\delta_{ik}\delta_{jl} + \delta_{il}\delta_{jk}\right) + \Pi_{44}\left(\delta_{ij}\delta_{kl} + \delta_{ik}\delta_{jl} + \delta_{il}\delta_{jk}\right) \tag{5}$$

where, Π_{11}, Π_{12} and Π_{44} represent the longitudinal, transverse, and shear piezoresistivity coefficients, respectively. Consequently, the electrical resistivity in 3D becomes a stress-dependent second-order tensor, where the components vary based on the piezoresistivity tensor Π_{ijlk}. Expanding Equation (3), the electrical resistivity components take the following form:

$$\rho_{ij} = \begin{cases} \rho_0\left(1 + \Pi_{11}\sigma_{ii} + \Pi_{12}\left(\sigma_{jj} + \sigma_{kk}\right)\right); & i = j \\ \rho_0\Pi_{44}\sigma_{ij}; & i \neq j \end{cases} \tag{6}$$

Assuming an isotropic piezoresistivity tensor, only 2 coefficients need to be defined as the shear coefficient, $\Pi_{44} = (\Pi_{11} - \Pi_{12})$.[29] In Section S1 and Figure S1 (Supporting Information), the influence of Π_{12} on the piezoresistive behavior of the material is delineated. Equation (3) is subsequently incorporated into the overall definition of electrical resistance, Equation (1).

When a large strain is applied to the bulk composite material, the cross-sectional area changes depending on its Poisson's ratio (ν). Accounting for the geometric nonlinearities due to the Poisson effect under mechanical loading, the transverse strains of an isotropic solid ($\varepsilon_{22} = \varepsilon_{33} = \varepsilon_t$) take the general form $\varepsilon_t = (1 + \varepsilon_{11})^{-\nu} - 1$.[30] Note that, by applying the Maclaurin series expansion to the first order of strain, $\varepsilon_t = -\nu\varepsilon_{11}$. The instantaneous cross-sectional area is then defined as $A_k = A_0\ (1 + \varepsilon_{11})^{-2\nu}$. Therefore, the electrical resistance evolution of the piezoresistive material along the loading direction, Equation (1), is expressed in the general form as:

$$R_{11} = \rho_0\frac{L_0}{A_0}\left(1 + \frac{\Delta\rho_{11}(\sigma_{11})}{\rho_0}\right)(1 + \varepsilon_{11})^{1+2\nu} \tag{7}$$

where, ρ_0 represents the electrical resistivity of the unstrained material, while L_0 and A_0 denote the length and area of the specimen in the unstrained state, respectively. ε_{11} refers to the engineering compressive or tensile strain experienced by the material in the loading direction. Equation (7) illustrates both the geometric and constitutive influences on the electrical resistance during mechanical deformation. Notably, a mere alteration in geometry can induce a piezoresistive response, as observed in most metals that do not demonstrate changes in electrical resistivity. However, composites predominantly exhibit constitutive effects, surpassing geometric ones, due to the interaction between conductive fillers/fibers and the matrix at the microstructural level.[22,23]

2.1.1. Piezoresistive Modeling of Elastic Composites

In real-time monitoring applications, the piezoresistive response is typically described in terms of the fractional change in electrical resistance $\frac{\Delta R_{11}}{R_0}$, where ΔR_{11} represents the change in resistance along the loading direction and R_0 is the initial resistance when strain $\varepsilon_{11} = 0$.

Within the elastic regime, albeit accounting for large strain, this can be formulated as:

$$\frac{\Delta R_{11}}{R_0} = \left(1 + \frac{\Delta\rho_{11}(\sigma_{11})}{\rho_0}\right)(1 + \varepsilon_{11})^{1+2\nu} - 1 \tag{8}$$

Applying the Maclaurin series expansion of Equation (8) to the first order of strain reveals that the piezoresistive response corresponds to the widely recognized formulation for small strain.[5]

$$\frac{\Delta R_{11}}{R_0} = \frac{\Delta\rho_{11}(\sigma_{11})}{\rho_0} + \varepsilon_{11}(1 + 2\nu) \tag{9}$$

In electronics and sensor technology, the strain sensitivity of active sensors is often quantified using a parameter called the Gauge Factor (GF).[31,32] The GF measures how much the electrical resistance of a sensor/smart material changes in response to applied mechanical strain or deformation. Dividing Equation (9) by engineering strain ε_{11}, the GF of piezoresistive composites exhibiting linear elastic behaviour under uniaxial stress takes the following form:

$$GF\ \frac{1}{R_0} \overset{\text{def}}{=} \frac{\Delta R_{11}}{\varepsilon_{11}} = \Pi_{11}E + 1 + 2\nu \tag{10}$$

In this equation, E and ν represent Young's modulus and Poisson's ratio of the piezoresistive material respectively. The GF, as defined in Equation (10), elucidates the mechanical, geometrical, and microstructural contributions to the piezoresistive response of the material. It encapsulates the key parameters that determine the strain sensitivity to external mechanical stimuli: Π_{11}, E, and ν. Furthermore, Equation (10) emphasizes that while the GF is unaffected by stress within the elastic regime, it may be influenced by nonlinear constitutive effects, such as $\Pi_{11}(\sigma_{ij})$ or $E(\sigma_{ij})$.

2.2. Piezoresistive Modeling of Elastoplastic Lattice Composites

The piezoresistive behavior of lattice materials isn't solely determined by the characteristics of the parent material; it's also

influenced by their architectural design. The arrangement of ligaments within the lattice material forms complex pathways for electrical current, which govern the piezoresistive effects. Analogous to dense materials, the electrical resistivity of lattice materials ρ^*_{ij}, connects the electric field to the electric current density, as described by the general definition of electric conduction law:

$$\Phi_i = \rho^*_{ij}\left(\sigma^*_{ij}, T\right)\bar{J}_j \tag{11}$$

where, $\bar{J}_j$ represents the effective macroscopic electric current density, equivalent to the average electric current density J_j within the domain Ω. In 3D, this implies a volume average, while in 2D, it implies an area average. The $\bar{J}_j$ is defined as:

$$\bar{J}_j = \frac{1}{|\Omega|}\int_{\Omega} J_j dV = \frac{1}{|\Omega|}\int_{\partial\Omega} J_j n_i x_i dS \tag{12}$$

where, n_i represents the outward normal to the domain, and x_i denotes the material point within the volume V enclosed by Ω. The electrical resistivity of lattice material can be formulated following the definition for dense material provided by Equation (3), as

$$\rho^*_{ij} = \rho^*_0\left(\delta_{ij} + \frac{\Delta\rho^*_{ij}\left(\sigma_{ij}\right)}{\rho^*_0}\right) \tag{13}$$

where, ρ^*_0 represents the electrical resistivity of the lattice material under unrestrained conditions. Under undeformed conditions, Φ_0 can be enforced on both dense and lattice materials, yielding $\Phi_0 = \rho^*_0\ \bar{J}_0 = \rho_0 J_0$. This relationship leads to:

$$\bar{\varrho} \overset{\text{def}}{=} \frac{\rho^*_0}{\rho_0} = \frac{J_0}{\bar{J}_0} \tag{14}$$

where $\bar{\varrho}$ represents the relative electrical resistivity, indicating the impact of the architecture of the lattice material on electric current flow within the domain. $\bar{\varrho}$ is consistently greater than 1 for lattice materials. When the solid volume fraction of the lattice material reaches 1, $\bar{\varrho}$ equals 1. If it exhibits orthotropy $\bar{\varrho}$ becomes $\bar{\varrho}_i$, denoting resistivity values along coordinate directions so that the electrical resistivity of lattice material , ρ^*_{ij}, can be generalized as follows:

$$\rho^*_{ij} = \rho_0\left(\delta_{ij}\bar{\varrho}_i + \frac{\Delta\rho^*_{ij}\left(\sigma_{ij}\right)}{\rho_0\bar{\varrho}_i}\right) \tag{15}$$

Drawing parallels with bulk materials, the relationship between the fractional change in electrical resistivity of lattice materials $\frac{\Delta\rho^*_{ij}}{\rho^*_0}$ and mechanical strain or stress can be established through the fourth-order piezoresistivity tensor Π^*_{ijlk}, so that the electrical resistance of lattice material R^*_{11}, can be written as follows:

$$R^*_{11} = R^*_0\bar{\varrho}\left(1 + \Pi^*_{11}\sigma^*_{11}\right)\frac{1+\varepsilon_{11}}{\left(1-\varepsilon_{11}\nu^*_{12}\right)\left(1-\varepsilon_{11}\nu^*_{13}\right)} \tag{16}$$

where $R^*_0 = \rho^*_0\ \frac{L^*_0}{A^*_0}$, is the electrical resistance of a lattice material in the unstrained state with a length-to-area ratio equal to $\frac{L^*_0}{A^*_0}$. The ν^*_{12} and ν^*_{13} are the Poisson's ratios of lattice material which consider changes in cross-section. The σ^*_{11} denotes the engineering stress in lattice material and Π^*_{11} denotes the piezoresistivity coefficient of the lattice along direction 1. Therefore, Π^*_{11} considers the influence of architectural design and parent material characteristics on the piezoresistive response of lattice material, mirroring Π_{11} for parent material in the elastoplastic domain.

2.2.1. Piezoresistive Modelling of Elastic Lattice Composites

To assess the influence of architecture in the elastic regime, the properties of lattice material are typically normalized with those of dense materials, as proposed by Gibson-Ashby for mechanical properties,[33] leading to the definition of the relative piezoresistive factor $\bar{\Pi}$:

$$\bar{\Pi} \overset{\text{def}}{=} \frac{\Pi^*_{11}}{\Pi_{11}} \tag{17}$$

where Π^*_{11} is the piezoresistive factor of lattice material under uniaxial loading. A detailed analytical description of the nature of $\bar{\Pi}$ is provided in Section S2 (Supporting Information). In analogy with bulk materials (see, Equation (9)), the fractional change of electrical resistance in the elastic regime of lattice materials can be expressed as:

$$\frac{\Delta R^*_{11}}{R^*_0} = \bar{\Pi}\,\Pi_{11}\sigma^*_{11} + \varepsilon_{11}\left(1 + \nu^*_{12} + \nu^*_{13}\right) \tag{18}$$

Equation (18) can be simplified by leveraging the 2D nature of the lattice material. According to Gibson,[34] the out-of-plane Poisson's ratio of planar lattice material ν^*_{13}, can be derived from the relationship between its in-plane stiffness (E^*_1) and out-of-plane stiffness (E^*_3), specifically $\nu^*_{13} = \frac{E^*_1}{E^*_3}\ \nu^*_{31} = \frac{E^*_1}{E^*_3}\ \nu$. In planar structures, E^*_1 is typically very small compared to the out-of-plane stiffness E^*_3. Therefore, Equation (18) assumes the following form for planar lattice materials:

$$\frac{\Delta R^*_{11}}{R^*_0} = \bar{\Pi}\,\Pi_{11}\sigma^*_{11} + \varepsilon_{11}\left(1 + \nu^*_{12}\right) \tag{19}$$

In line with dense materials, as delineated in Equation (10), the gauge factor for planar lattice materials GF^*, in the linear elastic regime can be expressed as:

$$GF^* = \bar{\Pi}\ \bar{\mathrm{E}}\,\Pi_{11}\mathrm{E} + 1 + \nu^*_{12} \tag{20}$$

where $\bar{E} = \frac{E^*_1}{E}$ represents the relative modulus of the lattice structure. The piezoresistive behavior of lattice materials is intricately tied to their architectural parameters ($\bar{\Pi}$, ν^*_{12}, $\bar{\mathrm{E}}$) and the intrinsic piezoresistive and mechanical properties of the parent material (Π_{11}, E). Notably, $\bar{\Pi}$ and the relative modulus $\bar{\mathrm{E}}$ typically fall below 1, resulting in piezoresistive lattice materials often exhibiting a gauge factor lower than that of the parent materials. Furthermore, in this scenario, GF^* remains unaffected by stress in

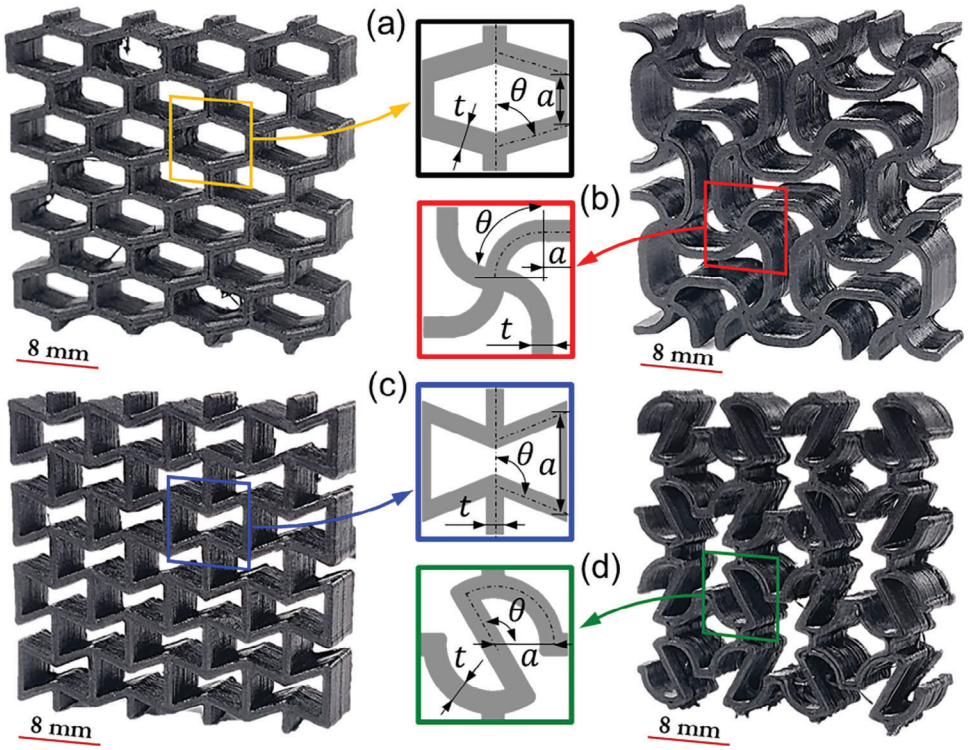

Figure 1. Additively manufactured 3 wt.% CNT-reinforced Polyetherimide lattice composites for a relative density $\bar{\rho} = 30\%$, featuring Hexagonal a), I-shaped b), Re-Entrant c), and S-shaped d) configurations. The middle column displays the geometric models illustrating the architectural parameters of various unit cell topologies.

the elastic domain, allowing for its comparison to that of the parent material using scaling laws commonly applied in mechanical properties analyses. However, piezoresistive lattice materials may demonstrate a GF^* higher than the parent material if the nonlinear effects come into play. For instance, constitutive nonlinearities might stem from the parent material's nonlinear piezoresistivity coefficient, denoted as $\Pi(\sigma_{ij})$, while contact nonlinearities could arise from the formation of new conductive pathways due to the compression-induced contact percolation among cell walls in architectures like the I-Shaped lattice.

3. Materials and Methods

3.1. Additive Manufacturing

The Apium P220 FFF 3D printer was employed to produce both lattice and fully dense (bulk) specimens using PEI filament feedstock reinforced with 3 wt.% CNTs. This PEI/CNT filament was specially developed in-house utilizing a single screw extruder, blending commercially sourced PEI granules from Eurotech as ULTEM 1000 (density: 1.27 g cm^{-3}; Molecular Weight: 592 g mol^{-1}; glass transition temperature: 217 °C) with CNTs from Nanokomp (industrial-scale multi-walled CNTs with a minimum of 90% carbon purity, diameters of 5 to 15 nm, and lengths of 1.5 to 2 µm). Further details on the PEI/CNT filament manufacturing process can be found in a previous study.[35] The optimization of additive manufacturing process parameters involved extensive testing to achieve superior mechanical performance of FFF-printed PEI/CNT lattice composites. This ensured excellent printability and consistent geometric dimensions for optimal outcomes. The process parameters are summarized in Table S1 in Supporting Information. To prevent out-of-plane failure, a layer height of 0.15 mm was selected, and a zone heater was placed just above the printer nozzle's printing surface. Before 3D printing, the PEI/CNT filament underwent a drying process at 60 °C for 2 h.

Bulk PEI/CNT compression and tension specimens were manufactured with an infill density of 100%, with the longitudinal direction of the bead consistently aligned with the loading direction. The PEI/CNT lattices with 4 distinct unit cell topologies possessing a relative density $\bar{\rho} = 30\%$, as shown in **Figure 1** were also fabricated. Each lattice composite measured 32 x 32 x 12 mm and was arranged in a 4 × 4-unit cell array to ensure a uniform mechanical response without being influenced by boundary or edge effects.[36] To prevent unexpected inter-bead damage, the ratio of bead-to-cell wall thickness was maintained at 2, following the methodologies outlined in our prior study.[33] The architectural parameters for each unit cell topology are summarized in Table S2 (Supporting Information). Notably, the S-shaped and I-shaped unit cell topologies were designed using the anti-chiral strategy, visually depicted in Figure 1. All geometries were generated using nTopology.

3.2. Experimental Methods

Quasi-static experiments were conducted using a Zwick-Roell Z050 universal testing machine, equipped with a 5 kN load cell,

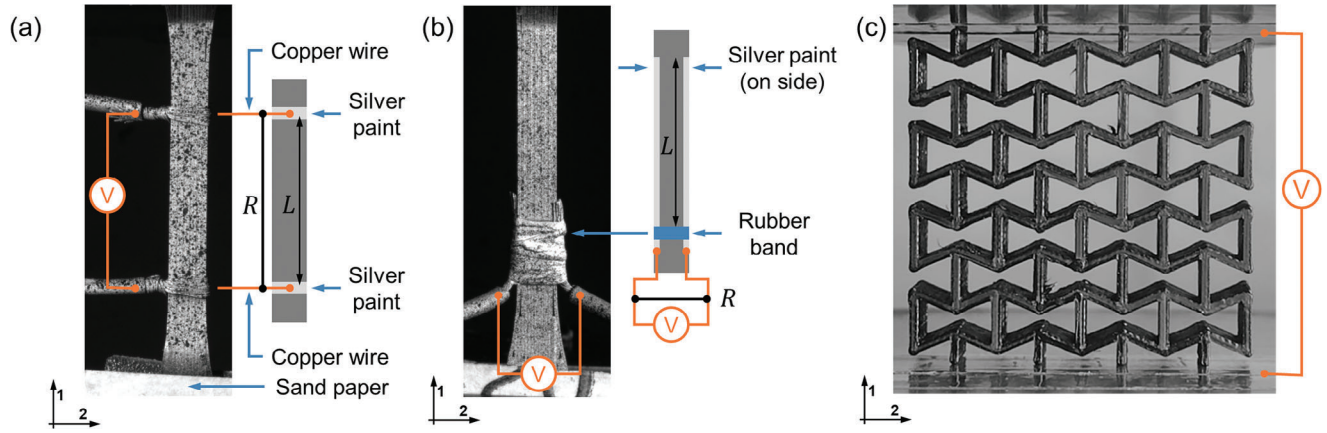

Figure 2. Experimental setup for measuring the piezoresistive response of parent and architected PEI/CNT lattice composites: a) Tensile test measuring electrical resistance along the gauge length aligned with the loading direction, b) Charles-Smith's test, a tensile test measuring electrical resistance orthogonal to the loading direction across the gauge section, and c) Compression test measuring the piezoresistive response of the lattice composite in the loading direction.

to evaluate the piezoresistive behavior of FFF-printed PEI/CNT bulk and lattice composites. Electrical resistance during the tests was monitored with a high-precision multimeter (Fluke 8846). The lattice composites underwent compression between 2 cylindrical steel plates at a speed of 2 mm min^{-1}, with the entire process recorded using a digital camera. To maintain quasi-static loading conditions, a strain rate of 10^{-3} s^{-1} was imposed. Deformations in tensile tests on bulk PEI/CNT composites were measured using the 2D Digital Image Correlation (DIC) technique.[37] Poisson's ratio of lattice composites was determined via an image processing algorithm developed using a Matlab script, tracking axial and transverse displacements during compression. Three specimens of each configuration were tested to ensure the experimental results' repeatability.

The piezoresistive properties of bulk PEI/CNT composite were determined by correlating electrical resistance signals observed in specific directions with mechanical behavior, as described in Equation (6). To assess Π_{11}, a uniaxial tensile test (ASTM D638) was conducted, measuring electrical resistance along the gauge length (as depicted in **Figure** 2a). The two-wire method was employed, with electrodes connected across the gauge length using silver paint to minimize contact effects. Π_{11} was indirectly obtained from the history of electrical resistance by rearranging Equation (7), assuming a uniaxial stress state ($\sigma_{22} = \sigma_{33} = 0$) and isotropic piezoresistive behaviour:

$$\Pi_{11} = \frac{1}{\sigma_{11}}\left(\frac{R_{11}}{R_0}\left(1+\varepsilon_{11}\right)^{-(1+2\nu)} - 1\right) \tag{21}$$

Similarly, the piezoresistive behavior under compression was determined using the same approach, and silver paint was applied between the circular faces of the cylindrical specimens. Π_{12} was evaluated by conducting a uniaxial test (ASTM D638) where electrical resistance was measured perpendicular to the gauge length (R_{22}), following Charles-Smith's experimental setup.[27] Silver paint was applied to the lateral faces of the specimen, and electrodes were secured with a rubber band (as shown in Figure 2b). Π_{12} was indirectly derived from the history of electrical resistance by rearranging Equation (7) where the electrical resistivity ρ_{22} was defined under the assumption of uniaxial stress state in the gauge section ($\sigma_{22} = \sigma_{33} = 0$) and isotropic piezoresistive behaviour governed by Equation (6):

$$\Pi_{12} = \frac{1}{\sigma_{11}}\left(\frac{R_{22}}{R_0}\left(1+\varepsilon_{11}\right) - 1\right) \tag{22}$$

During compression tests, the piezoresistive responses of lattice composites were monitored between 2 conductive stripes affixed over the compressive plates (as shown in Figure 2c). Tensile tests were conducted with sandpaper between the grippers and specimen to prevent slipping and current leakage through the grippers, while the compressive plates were fully insulated from the surrounding environment.

3.2.1. Infrared Thermal Imaging

The lattice composites were placed between conductive stripes connected to a 24V–45 W power supply and monitored for 2 s using a Flir X6900sc high-speed thermal imaging camera (20 Hz) at various specified compression strain levels (see Supplementary Information, Figure S2 (Supporting Information) for the experimental setup). The high current passing through the lattice composite ligaments from the conductive stripes induces Joule heating. This brief monitoring period allowed for the visualization of rapid heating specifically within the ligaments conducting the electric current. Areas not traversed by the current experience slower temperature increases, as heat spreads solely through thermal conduction. Consequently, the transient temperature mapping aligns with the paths of electric current within the lattice composite.

3.3. Finite Element Modeling

A multiscale multiphysics FE analysis for lattice composites needs to integrate mechanical and piezoresistive nonlinearities (constitutive, geometrical and contacts nonlinearities) and the interaction between macroscale architecture with local mechanical

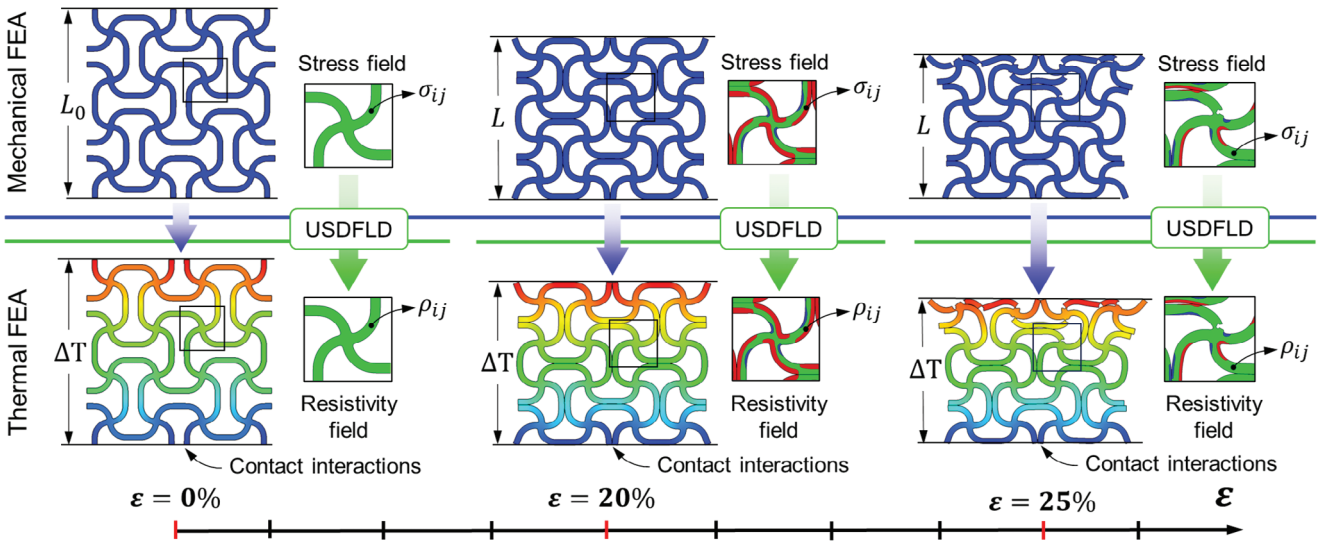

Figure 3. Methodology for the piezoresistive finite element analysis: Electrical resistivity was calculated using an electrical-thermal analogy within a steady-state thermal analysis, synchronized with the time steps of the mechanical analysis. The local electrical resistivity field was updated based on the stress field obtained from the mechanical analysis via thermal analysis, employing the USDFLD subroutine to define the piezoresistive response of the parent PEI/CNT composite.

and electrical attributes. Given that no commercial software provides comprehensive integration, this study proposes an FE modeling methodology within the Abaqus environment that couples mechanical and electrical analyses through external coding. This script facilitates predicting the evolution of the electrical resistivity field within the parent PEI/CNT composite considering a 3D stress state, as Equation (6) describes. The methodology begins with an independent mechanical FE analysis to evaluate the mechanical response. Subsequently, electrical FE analyses are conducted on the deformed shapes of parent and lattice composites, as predicted by the mechanical analysis for each respective case at every numerical simulation time step. The electrical resistivity of the parent PEI/CNT composite is correlated with stress fields using a user-defined subroutine (USDLFD) within Abaqus. The piezoresistive response is then reconstructed by determining the electrical resistance in each electrical simulation and associating it with stress-strain values from the corresponding mechanical analysis step. Further details regarding the FE models are discussed in the following section, while **Figure 3** offers an overview of the proposed methodology.

3.3.1. Mechanical Behavior Modeling

The mechanical constitutive response of the parent PEI/CNT composite was simulated using the damage-plasticity model developed by Lubliner, chosen for its versatility in modeling various quasi-brittle composites like reinforced concretes and composite.[36,38] This model, known as Concrete Damaged Plasticity (CDP) in the Abaqus environment, employs a combined Drucker-Prager and Rankine yield surface calibrated with uniaxial tension and compression yield stresses of FFF-printed bulk samples, detailed in Section 4.1. To govern the evolution of the yield surface, isotropic hardening variables are introduced via a non-associated flow rule with a negligible dilation angle, ensuring incompressible inelastic deformation, maintaining the convexity of the yield surface, and eliminating dependence on the third deviatoric stress invariant. Additionally, the compressive biaxial yield stress is assumed equal to the uniaxial one. The plasticity model's constitutive parameters are summarized in Table S3 (Supporting Information). Both tension and compression stress-strain data in the plastic regime are prescribed according to experimental tests, ensuring a strain-softening response without failure in compression and hardening with damage in tension. Stress degradation in tension post-failure is determined by a scalar damage variable (d_t) ranging from 0 (undamaged) to 1 (fully degraded material), expressed as:

$$\sigma_{11} = \left(1 - d_t\right) E \left(\varepsilon_{11} - \tilde{\varepsilon}_{11}^{pl}\right) \tag{23}$$

where E is Young's modulus of the material and $\tilde{\varepsilon}_{11}^{pl}$ is the equivalent plastic strain. A brief description of the damage model is provided in Section S3 (Supporting Information). and the damage model parameters are summarized in Table S4 (Supporting Information).

Plane strain finite element analysis (FEA) on lattice composites was conducted. The planar sections of lattice composites were imported from nTopology to the Abaqus environment as deformable planar surfaces and then subjected to compression assuming plane strain conditions. Additionally, the compressive plates were modeled as planar plates (considering steel's properties) and positioned above and below the lattice composites to mimic electrical interaction between the compressive plates and the lattice composite, replicating the experimental test setup where the multimeter pins were wired to the conductive strips on compressive plates as shown in Figure 2c. The plates' length exceeds the lattice composite length to ensure uniform compression when the lattice composite loses its integrity. A 4-node bilinear plane strain quadrilateral element with reduced

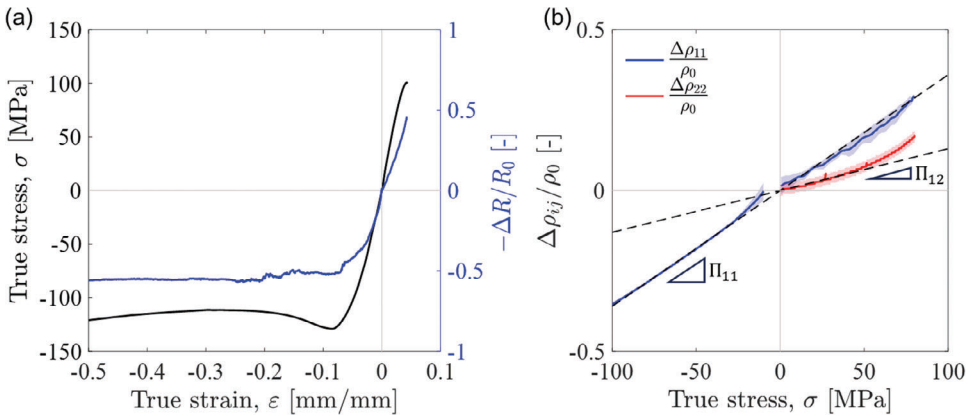

Figure 4. Measured piezoresistive behavior of parent PEI/CNT composite under uniaxial tension and compression: a) Stress-strain and piezoresistive response. b) Calibration of piezoresistivity factors for parent PEI/CNT composite. The dotted lines show the calibrated piezoresistivity parameters: Π_{11} and Π_{12}.

integration and hourglass control (CPE4R) was selected with an average mesh size of 0.1 mm. Abaqus/Explicit solver was utilized for the FE analysis. All contact interactions were modeled, defining normal and tangential contact behavior with friction properties based on a penalty factor of 0.1 and unilateral hard contact (separation after load removal).

3.3.2. Electrical and Piezoresistive Modeling

The electrical analysis utilized the Abaqus steady-state heat-transfer module, leveraging the analogy between electrical and thermal conduction equations. This thermal-electrical analogy allows for the substitution of all thermal properties with an appropriate set of electrical equivalents.[39] Following each step of the mechanical FE analysis, the deformed FE model of the compressed lattice composite was exported and sequentially imported into Abaqus for steady-state thermal simulations. Stress fields and element status information were stored accordingly. Automation of the element deletion procedure was achieved using a Python script: it reads the element status file from the mechanical analysis at each time step and subsequently deletes failed elements. Electrical interaction between the lattice composite and the contact surfaces formed between cell walls was modeled by defining electrical contact interactions in Abaqus. A stepwise function was used to model the contact conductance at the interface between cell walls, with extremely high conductance when the gap is zero and zero conductance when clearances are present. Both conductive plates and lattice composites were meshed with a 4-node plane strain thermally coupled quadrilateral element (CPE4RT), featuring bilinear displacement and temperature, reduced integration, and hourglass control. Electrical resistance was determined by evaluating the electrical current ($\bar{J}_1$) at the boundary due to the enforced potential difference through a homogenized electric field (Φ_1) along the compression direction, with a value of 0 at the lower end and 1 at the upper end, as shown in Figure 3. The electrical conductivity tensor associated with the parent composite was updated in each simulation according to Equation (6). Stress fields were imported into the thermal analysis environment using the Abaqus subroutine (USDLFD), enabling stress interaction with the electrical resistivity tensor (assuming a plane strain condition in mechanical analysis, i.e., ρ_{13} and ρ_{23} are zero).

4. Results and Discussion

4.1. Mechanical and Piezoresistive Performance of PEI/CNT Parent Composites

The quasi-static mechanical behavior of the FFF-printed PEI/CNT parent composite exhibits distinct characteristics. When subjected to tensile loading, it displays a brittle response, whereas, under compression loading, it shows ductile behavior, as illustrated in **Figure** 4a. The yield stress differs between compression and tensile tests: the compressive yield stress, σ_{CS}, is estimated to be 95 MPa, while the tensile yield stress, σ_{TS}, is estimated to be 85 MPa. Interestingly, Young's modulus, E, remains consistent in both tension and compression, measuring 3368 MPa, and Poisson's ratio is determined to be 0.3596 through DIC analysis. The composite's tensile strength and fracture strain ε_f are measured at 105 MPa and 0.044, respectively. Compared to unreinforced PEI, the PEI/CNT composite demonstrates higher mechanical performance, with a 50% increase in Young's modulus and a 10% increase in strength due to the addition of 3 wt.% CNT, as summarised in Table S5 (Supporting Information). Further discussion on the influence of CNT on the properties of PEI can be found in the previous study.[35]

Additionally, the FFF-printed PEI/CNT bulk composite exhibits a coherent piezoresistive response under quasi-static loading. Electrical resistance decreases under compression and increases under tensile loading, as depicted in Figure 4a. This behavior stems from microscale interactions between CNTs within the PEI matrix: compressive stress reduces the distance between CNTs, enhancing tunneling effects and forming new conductive paths, thereby decreasing the overall resistivity of the PEI/CNT composite.[40] Conversely, a tensile stress state moves the CNTs apart, producing the opposite effect. It's noteworthy that under compression, PEI/CNT exhibits a shift in electrical resistance trend from decreasing to stable once the composite's stress

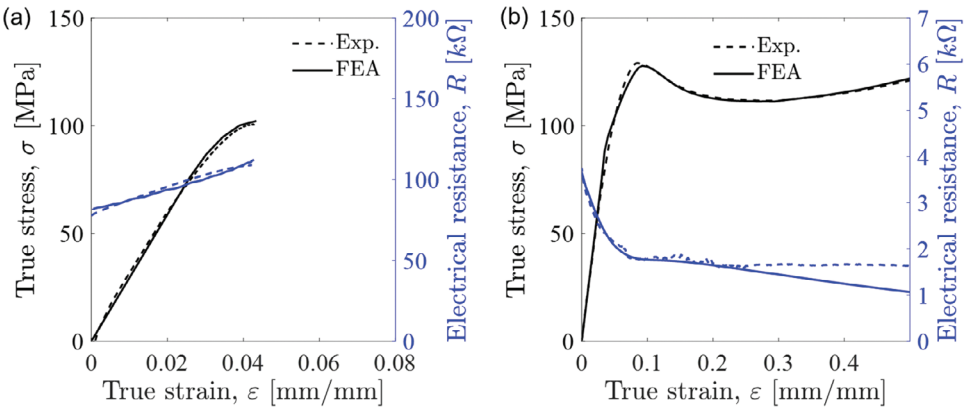

Figure 5. Numerical versus experimental stress-strain curves and electrical resistance evolution of parent PEI/CNT composite under uniaxial tension a) and compression b).

exceeds the peak value, and plastic deformation becomes predominant. This transition is typically attributed to the creation and destruction of conductive paths between CNTs.[40] Consequently, the microscale electrical interaction mechanism evolves as the deformation shifts from the elastic to the plastic regime. Moreover, the transverse deformation of the specimen due to Poisson's effect contributes to an increase in the distance between CNTs within the conductive network.[41]

The piezoresistive response of the PEI/CNT bulk composite in the loading direction is presented in Figure 4b under both compression and tensile loading, as well as along the transverse direction (Charles-Smith test). According to Equation (6), the slope of the fractional change in electrical resistivity versus the stress curve obtained from uniaxial loading conditions defines the piezoresistivity parameters Π_{11} and Π_{12}, measured according to Equations (21) and (22). Notably, Π_{11} remains consistent in tension and compression, measuring 0.0034 MPa^{-1}, whereas Π_{12} measures 0.0013 MPa^{-1}. The electrical resistivity of PEI/CNT composite under unstrained conditions, ρ_0, is calculated to be 22.8 Ωm or 0.045 S m^{-1} using Equation (7) for tensile samples and considering the associated cross-sectional area and length. The gauge factor of PEI/CNT under uniaxial tension measures ≈13.5, consistent with the analytical prediction using Equation (10), confirming the validity of the proposed model.

Numerical predictions of the piezoresistive response of the PEI/CNT composite were conducted through FE analysis. The predicted tensile and compressive behavior is depicted in **Figure 5**a,b, respectively. The FE predictions for mechanical behavior align well with experimental results under both loading conditions. Under tensile loading, the numerically predicted electrical resistance increases consistently, reflecting experimental observations. However, in the compression case, the numerical predictions of electrical resistance match experimental results up to moderate strains (≈25%) but diverge at larger strains, as illustrated in Figure 5b. This divergence is attributed to the interaction mechanism of CNTs within the polymer matrix. The piezoresistive model couples electrical resistivity with true stress, primarily driven by changes in the distance between CNTs.[40] Severe plastic deformation introduces an additional mechanism: the formation and disruption of conductive paths between CNTs,[40] resulting in nonlinear variations in piezoresistivity, i.e., $\Pi(\sigma_{ij})$. The predicted mechanical (stress-strain) and piezoresistive (electrical resistivity evolution) responses under tensile and compressive loading are also depicted in Figure S3 (Supporting Information). However, the numerical predictions remain consistent with experimental results up to the moderate strain, indicating that the second mechanism of CNT interaction becomes predominant only at large strains. Thus, the proposed piezoresistive model can be reliably employed to predict the piezoresistive behavior of lattice composites.

4.2. Piezoresistive Response of PEI/CNT Lattice Composites

The in-plane mechanical and piezoresistive behavior of FFF-printed PEI/CNT 2D lattices was measured under quasi-static compression loading. The deformation and failure patterns of lattices with $\bar{\rho}$ = 30% captured at different stages of loading along with macroscopic stress-strain and piezoresistive responses are shown in **Figure 6**: A (ε_{11} = 0.05) and B (Initial collapse).

The stress-strain curves exhibit an initial elastic phase, followed by a progressive brittle crushing regime dominated by ligament fractures. The in-plane compressive response of the PEI/CNT lattice composites is influenced by the unit cell topology and the parent composite's brittleness. The re-entrant and hexagonal lattices show a linear elastic regime whereas I-Shaped and S-Shaped lattice composites exhibit an extended nonlinear elastic regime, followed by a sudden drop in stress because of ligament fractures. The bending-dominated I-Shaped and S-Shaped architectures significantly enhance deformation, outperforming hexagonal and re-entrant lattices and effectively countering the brittleness of the parent PEI/CNT composite. Especially, the local rotation of the ligaments in the I-Shaped geometry turns out to be less critical than the S-Shaped lattice composite, facilitating a recoverable compressive response up to ε_{11} = 0.22. This behavior indicates that the nonlinear elastic response is reversible. Consequently, both lattice types can be utilized as nonlinear elastic sensors due to their excellent hysteretic behavior.

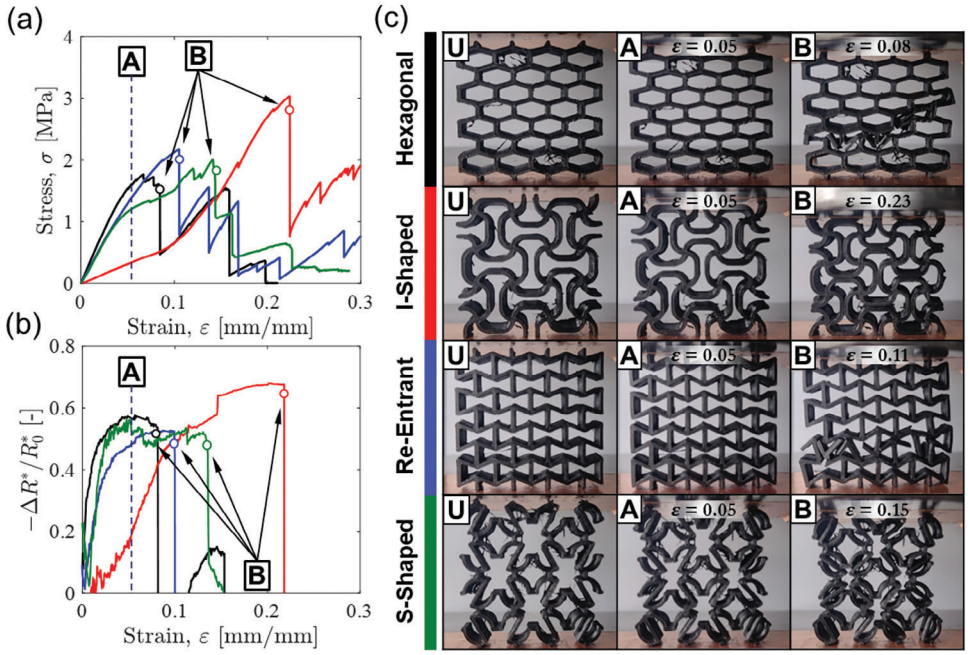

Figure 6. In-plane quasi-static compression behavior of PEI/CNT lattice composites with $\bar{\rho}$= 30%. Characteristic engineering stress-strain and piezoresistive responses with deformation maps at various stages of loading are shown: U (Undeformed), A ($\varepsilon = 0.05$), and B (Initial collapse).

The piezoresistive behavior of PEI/CNT lattice composites under compression shows electrical resistance decreases from the initial value (electrical resistance in the unstrained condition) to the critical value at which the lattice composites lose their integrity (strain at peak stress) (see, Figure 6b,c). Beyond these peak stresses, the electrical signal becomes extremely noisy because of ligament brittle failure, preventing a stable piezoresistive response in the collapse regime. Notably, the bending-dominated deformation behavior of the I-Shaped lattice composite counteracts the brittle nature of PEI/CNT, enabling an extended nonlinear piezoresistive response up to $\varepsilon_{11} = 0.22$. The piezoresistive responses indicate that the highest gauge factor, ≈10, is observed in the hexagonal and S-Shaped lattice composites, as summarized in **Table 1**.

The experimental results are subsequently compared with numerical predictions obtained through piezoresistive FE analysis, as shown in **Figure 7**. The predicted in-plane stress-strain responses and electrical resistance evolution of PEI/CNT lattice composites are consistent with the experimental results, especially before the collapse stage. The FE predictions confirm the appropriateness of the piezoresistive constitutive model proposed and the experimental strategy to calibrate its parameters. After the collapse stage, the numerical predictions have trouble following the brittle crushing response of the lattice composite because the new electrical paths are entirely dependent on the failure characteristics.

The piezoresistive response of PEI/CNT lattice composites can be better visualized in **Figure 8** in which the numerical, analytical, and experimental results are compared in terms of piezoresistive response. The slope of the linear trend line, which aligns with the analytical prediction, indicates the gauge factor. The numerical predictions and experimental results are consistent up to the collapse stress, besides capturing the nonlinear piezoresistive responses. I-shaped lattice composite exhibited a nonlinear piezoresistive response with 2 steps at $\varepsilon_{11} = 0.11$ and $\varepsilon_{11} = 0.16$. Both electrical resistance steps in piezoresistive response relate to the percolation of contacts between ligaments during the compression of lattices. The piezoresistive FE analysis aids in comprehending the interaction between electrical current flow and architecture, shedding light on the origins of nonlinear piezoresistive behavior (contact nonlinearities due to the percolation of contacts between ligaments).

Figure 9 describes clearly what happens at those strain/deformation stages during the compression of an

Table 1. In-plane piezoresistive properties of FFF-printed PEI/CNT lattice composites.

Lattice	$\bar{\rho}$		$\bar{\Pi}\,\bar{E}$		ν_{12}^*		GF^*		
Composite	Exp.	FEA	Exp.	FEA	Exp.	FEA	Exp.	FEA	Equation (20)
Hexagonal	9.3 ± 0.2	9.3	0.80 ± 0.03	0.75	+0.27 ± 0.01	0.25	9.9 ± 0.5	9.8	9.8
I-Shaped	11.9 ± 0.8	11.5	0.41 ± 0.06	0.22	−0.77 ± 0.03	−0.78	2.9 ± 0.9	2.8	2.8
Re-Entrant	18.1 ± 0.4	17.9	0.56 ± 0.01	0.53	−0.31 ± 0.02	−0.33	7.2 ± 0.3	6.7	6.7
S-Shaped	11.0 ± 0.6	10.7	0.96 ± 0.06	0.93	−1.83 ± 0.06	−1.94	10.1 ± 0.8	9.7	9.7

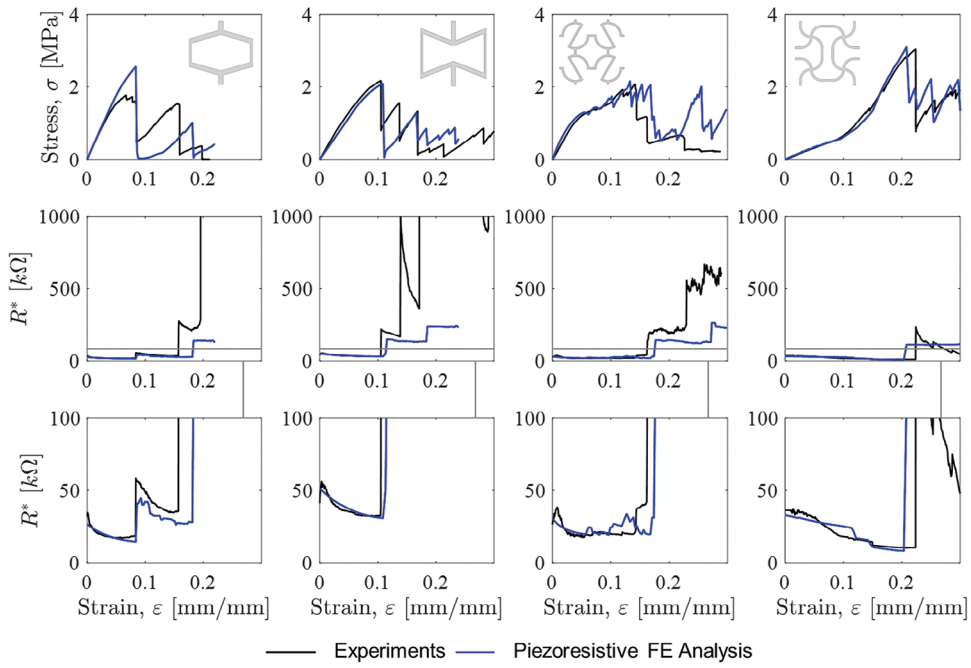

Figure 7. Comparison between experimental results and numerical predictions of in-plane stress-strain (top row) and piezoresistive (bottom 2 rows) responses of PEI/CNT lattice composites ($\bar{\rho} = 30\%$) under quasi-static compression.

I-shaped lattice composite. The piezoresistive FE analysis indicates that the horizontal ligaments of the I-shaped lattice composite at unstrained conditions are not crossed by electric current (see orange ellipses in Figure 9). As the compression loading increases, new electrical current paths are formed within the I-Shaped architecture due to the percolation of contacts between ligaments. Notably, the ligaments at the boundary of the lattice composite come in contact creating the first change in electrical resistance at $\varepsilon_{11} = 0.11$. Subsequently, the horizontal ligaments within the lattice (see red ellipses in Figure 9) come in contact as all contacts between ligaments in an I-shaped lattice composite percolate, generating the second change in electrical resistance at $\varepsilon_{11} = 0.16$. The numerical prediction clearly describes the changes in electrical resistance due to the formation of contacts exhibiting 2 steps whereas the experimental result shows first a smooth transition followed by the electrical resistance step when all the contacts in the lattice composite percolate, as shown in Figure 8. The higher sensitivity of the electrical contact interactions is due to the implemented electrical contact model: the contact conductance was modeled as a step function, creating an instantaneous change in contact conductance once the conductive ligaments come in contact. In reality, contact conductance is a pressure-dependent phenomenon, therefore, the experimental results indicate the local pressure was high enough to create a step change in electrical resistance only when all contacts between ligaments percolate. This approach aims to mimic electrical interactions as an on/off switch. While a triboelectric model could potentially enhance

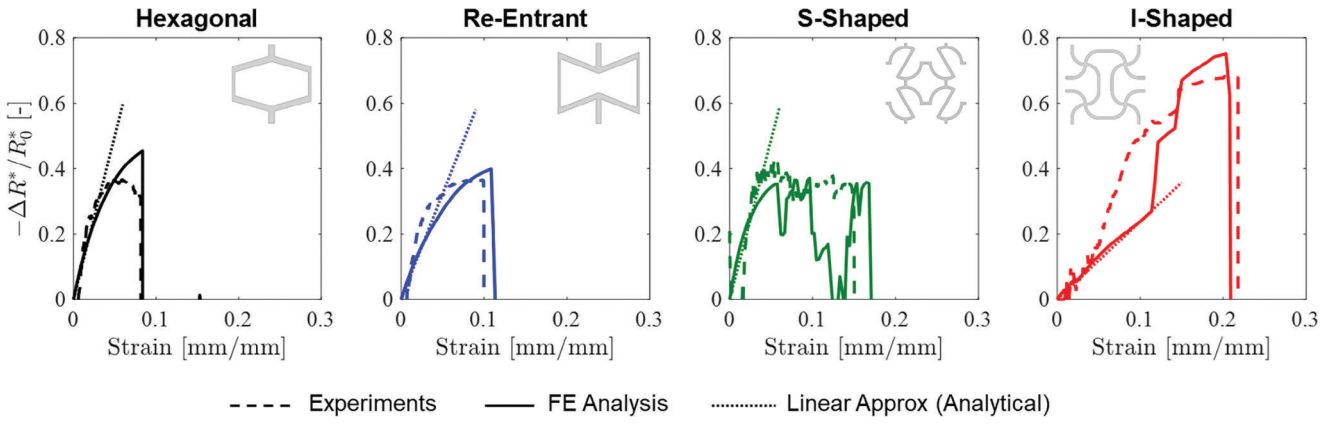

Figure 8. Comparison of numerical, experimental, and analytical results for the piezoresistive behavior of PEI/CNT 2D lattice composites under in-plane compression. Dashed lines indicate the initial slope.

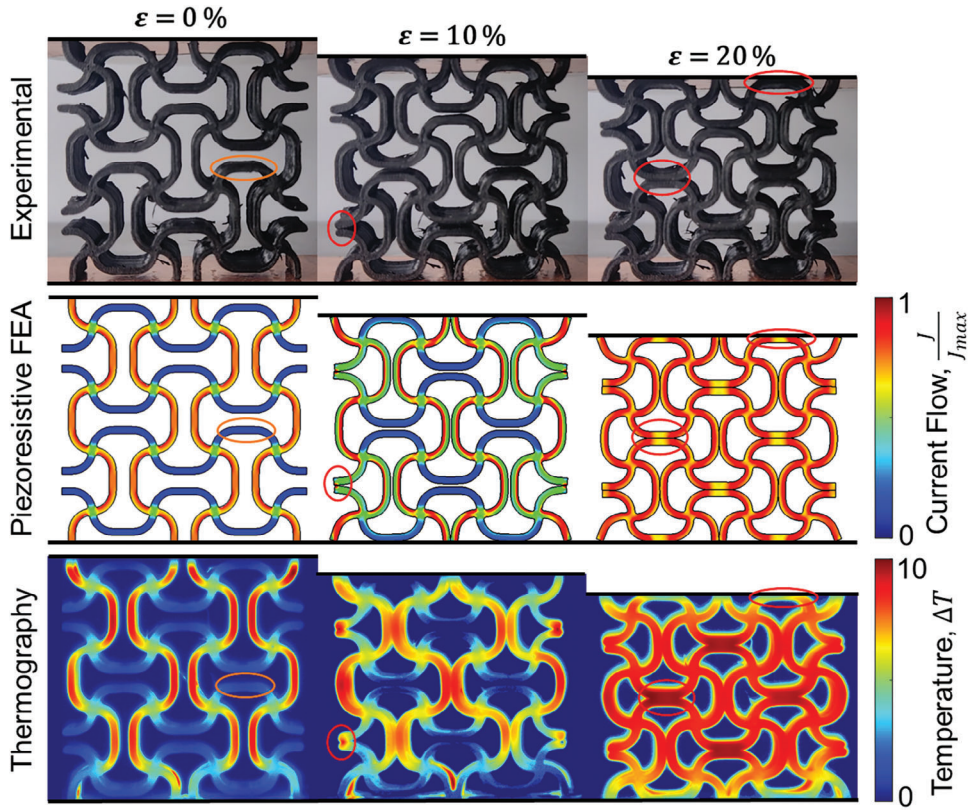

Figure 9. Comparison between experimental results and numerical predictions for an I-shaped PEI/CNT lattice composite under different compression strain levels. The top row presents deformation maps. The middle row displays piezoresistive FE maps, highlighting electric current paths within the lattice composite. Red ellipses mark ligament contacts that alter the current paths during compression, while orange ellipses indicate ligaments where the current does not flow in the unstrained state. The bottom row shows thermographic images of current flow paths, illustrating temperature increases due to the Joule heating effect (45 W–24 V after 2 s).

contact interactions, the current numerical model effectively predicts the macroscopic piezoresistive behavior of the lattices, aligning well with experimental results and demonstrating its robustness.

The numerically predicted electrical current paths were validated using thermography analysis, comparing the normalized resultant electric current density ($\frac{J}{J_{max}}$) within the lattice composites predicted using the FE model with the temperature maps generated connecting the I-Shaped lattice composite to a high-power supply, as shown in Figure 9. The temperature increases (ΔT) within ligaments due to the Joule heating effect generate 3 different maps, one for each strain stage, showing the changes in electric current paths during deformation because of the progressive change in contact percolations as predicted by the piezoresistive FE analysis. Furthermore, **Figure 10** illustrates the stress and electrical resistivity components within the unit cell of the I-Shaped lattice composite, showing that the compressed zone experiences a decrease in electrical resistivity as described by Equation (6). Video S1 (Movie S1), Supporting Information shows synchronized footage of stress-strain and piezoresistive responses, deformation maps, and electric current paths within the I-Shaped lattice composite, obtained from both experiments and simulation, including predictions of the electrical resistivity field.

4.2.1. Electrical Resistivity under Unstrained Conditions

Experimental and numerical results, summarized in Table 1, show the relative electrical resistivity of architected lattice composites change with the unit cell topology. The re-entrant lattice composite exhibits the highest value at 11.8, while the hexagonal lattice shows the lowest at 9.3. This variation is due to the interaction of the electric current with the architectures, as demonstrated in **Figure 11**.

The local electrical current density along the vertical (J_1) and transverse (J_2) directions within the material domain are illustrated, with dotted lines representing the average electrical current density ($\bar{J}_1$ and $\bar{J}_2$). The symmetric distribution of J_2 results in $\bar{J}_2 = 0$, indicating no macroscopic current flow in the transverse direction, whereas the asymmetric J_1 distribution results in $\bar{J}_1 \neq 0$, showing macroscopic current flow in the loading direction. A higher $\bar{J}_1$ corresponds to lower relative electrical resistivity. The J_1 distribution explains why the re-entrant lattice composite has the highest relative electrical resistivity value; the re-entrant lattice composite has a negative J_1 (current flows opposite to loading direction) in horizontal "V" ligaments, meaning the current flows toward the cell center and then comes back following the Re-entrant shape, generating an intricate path that counters the vertical current. Furthermore, Figure 11 shows that J_1

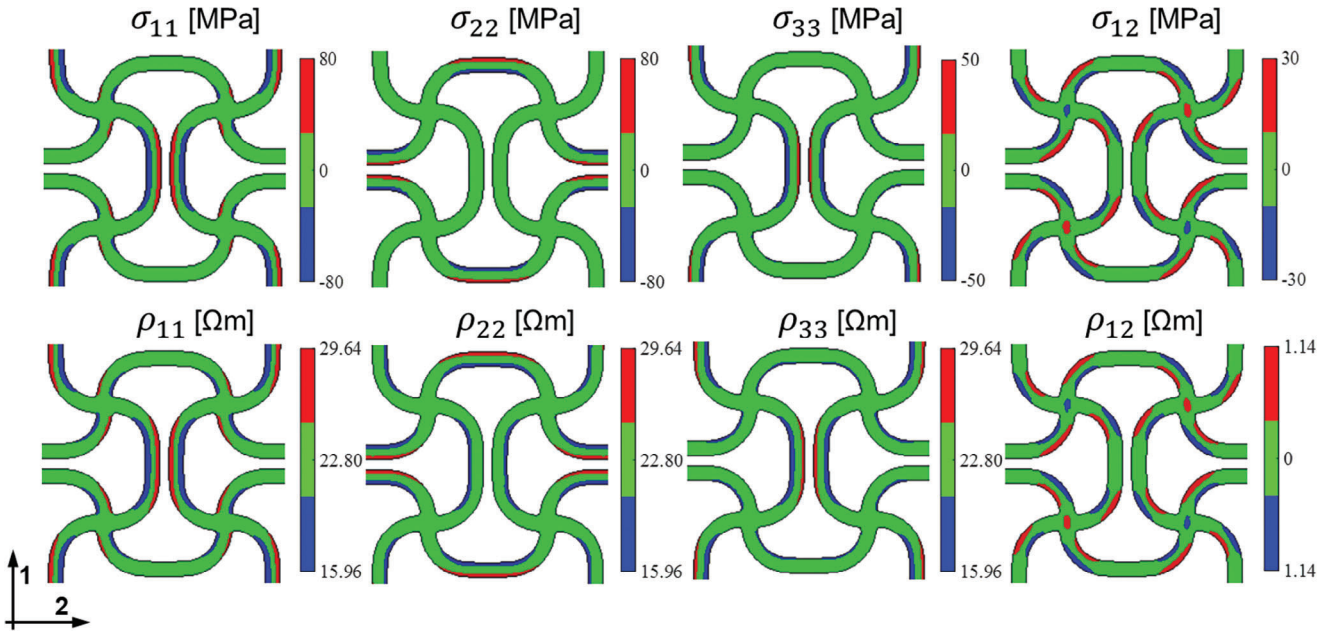

Figure 10. Predicted stress and electrical resistivity components in deformed I-Shaped PEI/CNT lattice composite at imposed macroscopic compression strain $\varepsilon_{11} = 0.05$.

locally reached the highest values in the I-Shaped and S-Shaped lattice composites, even though their average $\bar{J}_1$ values are not higher than those of the hexagonal lattice composites. This is because $\bar{J}_1$ is an average value negatively impacted by untraveled zones. The I-Shaped and S-Shaped lattice composites exhibit preferential current flow across vertical ligaments with no flow through horizontal ones, as shown in **Figure** 12. This is due to the electric current flowing along the shortest path, connecting the lower to the upper sides. Additionally, monitoring the piezoresistive response of these lattice composites only in the vertical direction minimizes the impact of damage or imperfections in the horizontal ligaments. Conversely, the hexagonal and re-entrant lattices have intricate architectures that force the electrical current to travel throughout the entire material domain, so imperfections or damage always affect the monitored current flow in the loading direction. The electric current flows are qualitatively validated using thermographic images showing temperature increases due to Joule heating, which align with piezoresistive FEA predictions, as shown in Figure 12.

4.2.2. Gauge Factor and Local Piezoresistive Response

Experimental and numerical results demonstrate an architecture-dependent gauge factor, as shown in Figure 8 (see, Table 1). This could be attributed to the local interaction among the electric current paths, the piezoresistive response of the parent composite, and the stress state. To demonstrate that, here we introduce the local gauge factor k_1. From a macroscopic

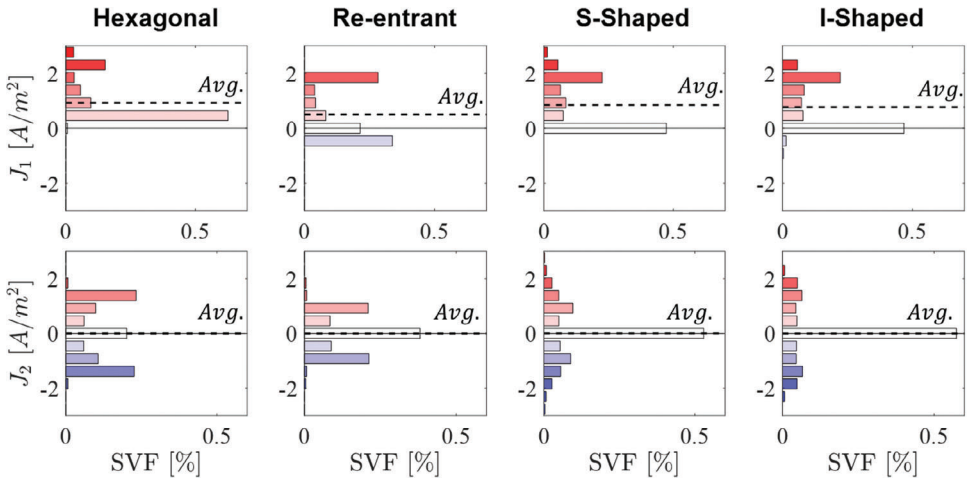

Figure 11. Electrical current density within PEI/CNT lattice composite in the loading direction J_1 and transverse direction J_2 versus the Solid Volume Fraction (SVF). The dotted line represents the average current density value, $\bar{J}_1$ and $\bar{J}_2$ respectively.

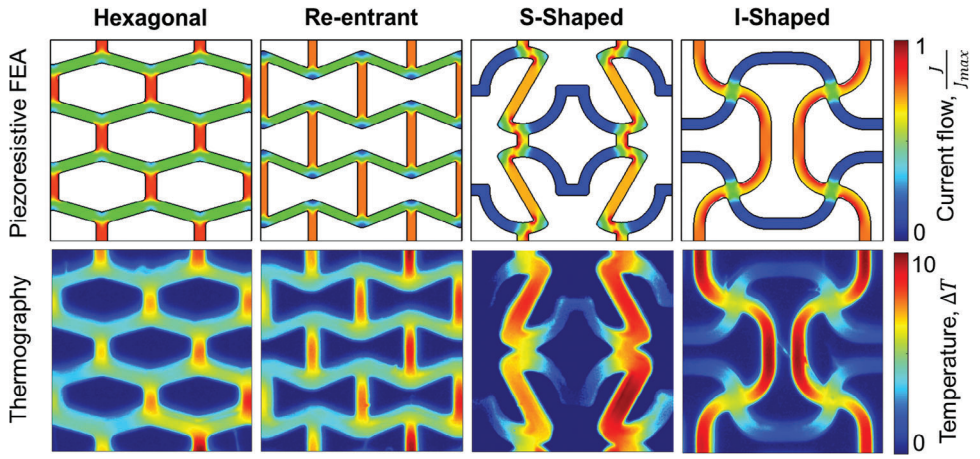

Figure 12. Electric current paths within the PEI/CNT lattice composites under unstrained conditions. The piezoresistive FE predictions are compared to thermographic images, which qualitatively illustrate the electric current paths by highlighting temperature increases caused by the Joule heating effect (45 W–24 V after 2 s).

point of view, the gauge factor is strictly dependent on the fractional change in electrical resistance at a given strain or the change in electrical current inside the lattice material, as suggested by

$$\frac{\Delta R_{11}^*}{R_0^*} = \frac{I_0^*}{I_1^*} - 1 = \frac{\bar{J}_0 A_0^*}{\bar{J}_1 A^*} - 1 \tag{24}$$

where I_0^* and I_1^* are the electrical currents traveling within lattice material measured at the boundary in unstrained and deformed conditions, respectively. Assuming the change in cross-sectional area is negligible, the piezoresistive response is dependent on the local change in electrical current density along the loading direction thus local gauge factor is defined as follows:

$$k_1 = \frac{J_0}{J_1} - 1 \tag{25}$$

Figure 11 highlights several aspects of piezoresistive interactions within the lattice, showing the k_1 values computed for each element of the FE model at a given macroscopic compression strain of $\varepsilon_{11} = 0.05$. The dotted line corresponds to the fractional change in electrical resistance measured at the boundary ($\frac{\Delta R_{11}^*}{R_0^*}$) and coincides with the average k_1 values ($\bar{k}_1$) within the lattice composite. k_1 reaches higher magnitude in high piezoresistive regions because of experiencing high local stresses; hence, the k_1 values are notably low in vertical ligaments, as in hexagonal central compressed ligaments (blue zones), and ligament edges, as in S-shaped lattice composites, where local stress concentrations exist. However, k_1 equals to zero negatively affects the lattice gauge factor, which occurs under 2 conditions: the parent composite is not deformed, or the electric flow does not travel across the stressed zones, as shown by blue zones in Figure 10 and by white zones in **Figure 13**. Therefore, the necessary condition to have a high GF^* for a lattice composite under compression is that the electric current must flow across high piezoresistive zones or zones with low k_1 values ($GF^* \cong \frac{\bar{k}_1}{\varepsilon_{11}}$). For instance, while the S-Shaped lattice composite exhibits the lowest k_1 values, its GF^* is comparable to the hexagonal lattice. This is because the S-Shaped architecture restricts current flow to the central ligaments, resulting in limited current flow in the edges, which are regions with the highest piezoresistive properties. Conversely, the hexagonal lattice composite facilitates electric current flow across its entire domain, especially in central ligaments which have the lowest k_1 values.

Furthermore, the flexural behavior of ligaments, inside the S-Shaped central ligaments (violet zones), mitigates the overall lattice composite's piezoresistive response. This occurs because the piezoresistive effect induced by tensile stress balances the effect of compressive stress, resulting in zones with the same $k_1 \approx 0$. Lattice composites with low stiffness, such as the I-Shaped configuration, do not experience significant stress within their ligaments because of high ligament mobility, resulting in near-zero $\bar{k}_1$ values.

4.3. Gauge Factors of Architected Lattice Composites

In comparison with piezoresistive composites enabled via additive manufacturing, both PEI/CNT parent and lattice composites exhibit remarkable gauge factors, especially when compared to other composites made of high-performance thermoplastic polymers like PEEK or PP, as shown in **Figure 14**. Therefore, the superior strength and stiffness, combined with high strain sensing ability, make PEI/CNT a good candidate for autonomous sensing lightweight lattice composites. Moreover, Figure 14 confirms the enhanced strain sensitivity of piezoresistive architected lattice composites compared to piezoresistive foams.

Both experimental and numerical results highlight that the gauge factor of lattice composites is lower than that of the parent composite, as inferred through Equation (20). This leads to the affirmation that the gauge factor of lattice composites ranges from that of the parent composite to lower values due to changes in relative density and architecture. This observed trend is also visible in other studies on piezoresistive FFF-printed lattice composites, as indicated by shaded areas in Figure 14, demonstrating that the nature of the piezoresistive behavior of parent

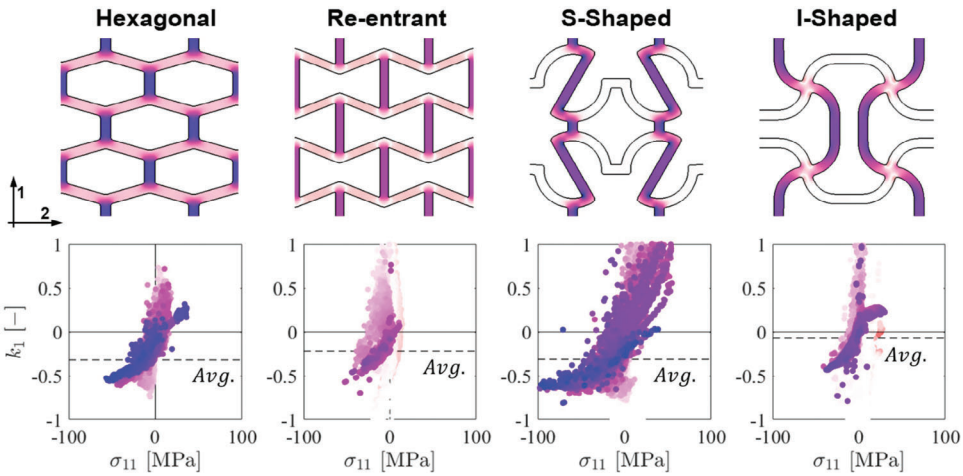

Figure 13. Local piezoresistive behavior of PEI/CNT 2D lattice composite under a macroscopic compressive strain $\varepsilon_{11} = 0.05$. The top row illustrates the electrical current density along the loading direction, J_1 under unstrained conditions. The bottom row depicts the distribution of the local gauge factor k_1 versus the local stress σ_{11} calculated for each element of the FE model. The color map indicates the spatial variation of $k_1$within the material. The dotted line represents the average change in electrical resistance ($\bar{k}_1$) at a given strain, which is proportional to the gauge factor of each lattice composite.

composites affects the y-position of shaded areas, whereas the architecture affects the width. A similar effect is typically observed in the mechanics of lattice composites, where stiffness, strength, and energy absorption characteristics vary from those of the composite to lower ones due to changes in the lattice composite's relative density and unit cell topology.[33] Therefore, the gauge factor of lattice composites may be framed as a relative property connected to relative density ($\bar{\rho}$), extending the concept of mechanical properties scaling laws to electrical ones.

$$\frac{\rho_0^*}{\rho_0} = \bar{\rho} = C_1 \ \bar{\rho}^{\beta_2} \tag{26}$$

$$\frac{GF^*}{GF} = \overline{GF} = C_2 \ \bar{\rho}^{\beta_2} \tag{27}$$

where C_1, C_2, β_1 and β_2 are the architecture-dependent parameters. Scaling laws for electrical resistivity have already been discussed in the literature,[55] while the gauge factor has never been highlighted before. This insight allows us to bridge the gap between material research and mechanics, enabling the design and optimization of lightweight piezoresistive structural materials. Consequently, the gauge factor may become a design requirement, predictable through scaling laws once the behavior of the parent composite and the

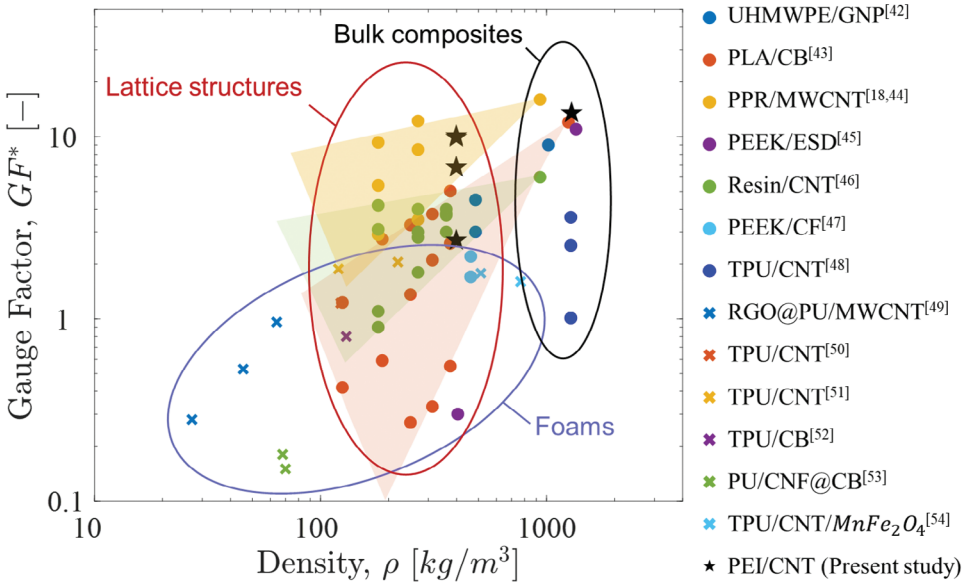

Figure 14. Gauge factors comparison of piezoresistive parent and lattice PEI/CNT composites with extant works (both foams and architected lattice composites).

architecture of the lattice composite is known, like mechanical properties.

5. Conclusion

This study provides significant insights into the development of additively manufactured autonomous sensing architected composites by seamlessly integrating analytical models, experimental data, and predictive finite element (FE) simulations. We systematically examined the in-plane mechanical and autonomous sensing behavior of FFF-printed 2D PEI/CNT lattice composites with 30% relative density, focusing on 4 distinct unit cell topologies under compressive loading. The findings reveal how architectural variations and parent composite properties govern the strain and damage sensitivity of piezoresistive lattice composites. Notably, the bulk PEI/CNT composite demonstrated exceptional mechanical performance, with a strength of 105 MPa, stiffness of 3368 MPa, and strain sensitivity, marked by a gauge factor of ≈13. Among the studied lattice architectures, the Hexagonal lattice, the stiffest, exhibited a gauge factor of ≈10, while the compliant I-Shaped lattice exhibited a gauge factor of ≈3.7. Stretching-dominated architectures like Hexagonal and Re-entrant lattices were stiff yet brittle, whereas bending-dominated designs like I-Shaped and S-Shaped lattices offered extended nonlinear elasticity, mitigating the brittleness of the parent composite while providing moderate deformation capacity. The significant strain sensitivity observed, particularly in Hexagonal, Re-entrant, and S-Shaped lattices, underscores the promising potential of these materials for advanced sensing applications.

The multiscale multiphysics FE model, implemented through a user-defined subroutine (USDFLD) in Abaqus, effectively captured the piezoresistive responses of the PEI/CNT lattice composites, accounting for material, geometric, and contact nonlinearities. The strong correlation between the FE predictions and experimental results validated both the proposed piezoresistive constitutive model and the experimental strategy used to calibrate the mechanical (CDP model) and piezoresistive parameters. Complementary thermography analysis further validated the model by confirming the predicted electric current paths, particularly within the I-Shaped and S-Shaped lattices, where preferential current flow across vertical ligaments under unstrained conditions aligned with the FE simulations. The nonlinear changes in electric current paths observed during compression in the I-Shaped lattice, driven by contact percolation between ligaments, further corroborated the model's accuracy. These insights reveal the critical role of aligning electric current paths with high piezoresistive zones to optimize gauge factors, paving the way for designing and optimizing lightweight, high-performance autonomous sensing materials across various engineering sectors.

The formulation of a closed-form expression for predicting the gauge factors of lattice composites, which incorporates both architectural and parent composite properties, showcases the elegance and utility of the piezoresistive modeling framework. The gauge factors observed in PEI/CNT parent and lattice composites, as shown in our Ashby chart analysis, indicate that these materials have potential for future autonomous sensing applications. Notably, the Ashby chart analysis suggests that the gauge factor of architected lattice composites can be predicted using a scaling law analogous to those for mechanical properties. These findings, together with the proposed multiscale FE model, unlock exciting new opportunities for the predictive design and optimization of piezoresistive materials for advanced applications.

Moreover, the impressive mechanical performance and high strain sensitivity of the PEI/CNT lattice composites underscore their potential as lightweight autonomous sensing materials for load-bearing applications. Future research should focus on scaling these composites for broader use and exploring their performance under diverse environmental conditions. Investigating the integration of these materials into real-world applications will be pivotal for transforming our insights into practical, smart technologies. This work not only advances the field of piezoresistive composites but also lays the groundwork for the development of intelligent, responsive materials with broad functional applications.

Supporting Information

Supporting Information is available from the Wiley Online Library or from the author.

Acknowledgements

Financed by the European Union-NextGenerationEU (National Sustainable Mobility Center CN00000023, Italian Ministry of University and Research Decree No.1033-17/06/2022, Spoke 11- Innovative Materials & Lightweighting), and National Recovery and Resilience Plan (NRRP), Mission 04 Component 2 Investment 1.5-NextGenerationEU, call for tender n. 3277 dated 30 December 2021. The authors declare no financial and non-financial competing interests in the subject matter or materials discussed in this article. The opinions expressed are those of the authors only and should not be considered representative of the European Union or the European Commission's official position. Neither the European Union nor the European Commission can be held responsible for them. SK would like to acknowledge the financial support through USyd-UofG Ignition Grants. S. K. gratefully acknowledges the support through the Vaibhav Fellowship awarded by the Department of Science & Technology, India [DST/IC/VAIBHAV/Award/2024/L-10].

Conflict of Interest

The authors declare no conflict of interest.

Data Availability Statement

The data that support the findings of this study are available from the corresponding author upon reasonable request.

Keywords

3D printing, architected cellular materials, infrared thermography, multiscale and multiphysics modeling, self-sensing composites

Received: July 7, 2024
Revised: September 10, 2024
Published online:

[1] J. Zhou, Y. Huan, L. Zhang, Z. Wang, X. Zhou, J. Liu, X. Shen, L. Hu, T. Qian, C. Yan, *Mater. Today* **2022**, *60*, 271.
[2] Q. Zheng, J. Lee, X. Shen, X. Chen, J.-K. Kim, *Mater. Today* **2020**, *36*, 158.
[3] Y. Yang, S. Zhang, Y. Ji, Y. Wei, J. Wang, X. He, *Mater. Today* **2024**, *74*, 167.
[4] H. Gao, J. An, C. K. Chua, D. Bourell, C.-N. Kuo, D. T. H. Tan, *Mater. Today* **2023**, *69*, 107.
[5] A. S. Fiorillo, C. D. Critello, S. A. Pullano, *Sens. Actuators, A* **2018**, *281*, 156.
[6] L. Duan, D. R. D'hooge, L. Cardon, *Prog. Mater. Sci.* **2020**, *114*, 100617.
[7] L. Zhang, J. Li, F. Wang, J. Shi, W. Chen, X. Tao, *Mater. Sci. Engineer.: R: Rep.* **2021**, *146*, 100629.
[8] S. Shen, Q. Zhou, G. Chen, Y. Fang, O. Kurilova, Z. Liu, S. Li, J. Chen, *Mater. Today* **2024**, *72*, 140.
[9] N. Luo, W. Dai, C. Li, Z. Zhou, L. Lu, C. C. Y. Poon, S. Chen, Y. Zhang, N. Zhao, *Adv. Funct. Mater.* **2016**, *26*, 1178.
[10] E. Davoodi, H. Montazerian, R. Haghniaz, A. Rashidi, S. Ahadian, A. Sheikhi, J. Chen, A. Khademhosseini, A. S. Milani, M. Hoorfar, E. Toyserkani, *ACS Nano* **2020**, *14*, 1520.
[11] D. Chen, Z. Han, J. Zhang, L. Xue, S. Liu, *Adv. Sci.* **2024**, *11*, 2400816.
[12] H. Abramovitch, M. Burgard, L. Edery-Azulay, K. E. Evans, M. Hoffmeister, W. Miller, F. Scarpa, C. W. Smith, K. F. Tee, *Compos. Sci. Technol.* **2010**, *70*, 1072.
[13] B. M. Gackowski, G. D. Goh, M. Sharma, S. Idapalapati, *Composites, Part B* **2023**, *261*, 110796.
[14] H. Tetik, Y. Wang, X. Sun, D. Cao, N. Shah, H. Zhu, F. Qian, D. Lin, *Adv. Funct. Mater.* **2021**, *31*, 2103410.
[15] Z. Wang, X. Guan, H. Huang, H. Wang, W. Lin, Z. Peng, *Adv. Funct. Mater.* **2019**, *29*, 1807569.
[16] Y. Li, S. Luo, M. Yang, R. Liang, C. Zeng, *Adv. Funct. Mater.* **2016**, *26*, 2900.
[17] C. E. Owens, G. H. McKinley, A. J. Hart, *Mater. Today* **2024**, *75*, 97.
[18] P. Verma, J. Ubaid, K. M. Varadarajan, B. L. Wardle, S. Kumar, *ACS Appl. Mater. Interfaces* **2022**, *14*, 8361.
[19] E. Davoodi, H. Fayazfar, F. Liravi, E. Jabari, E. Toyserkani, *Addit. Manuf.* **2020**, *32*, 101016.
[20] M. Panahi-Sarmad, M. Noroozi, M. Abrisham, S. Eghbalinia, F. Teimoury, A. R. Bahramian, P. Dehghan, M. Sadri, V. Goodarzi, *ACS Appl. Electron. Mater.* **2020**, *2*, 2318.
[21] J. Oliveira, V. Correia, H. Castro, P. Martins, S. Lanceros-Mendez, *Addit. Manuf.* **2018**, *21*, 269.
[22] Y. Fang, L.-Y. Li, S.-H. Jang, *Compos. Sci. Technol.* **2021**, *208*, 108757.
[23] G. Pal, S. Kumar, *Mater. Des.* **2016**, *89*, 129.
[24] A. Mora, P. Verma, S. Kumar, *Composites, Part B* **2020**, *183*, 107600.
[25] L. Quinteros, E. García-Macías, E. Martínez-Pañeda, *Comp. Methods Appl. Mech. Engineer.* **2023**, *407*, 115941.
[26] E. García-Macías, R. Castro-Triguero, A. Sáez, F. Ubertini, *Comp. Methods Appl. Mech. Engineer.* **2018**, *340*, 396.
[27] C. S. Smith, *Phys. Rev.* **1954**, *94*, 42.
[28] R. Hinchet, U. Khan, C. Falconi, S.-W. Kim, *Mater. Today* **2018**, *21*, 611.
[29] F. C. Buroni, E. García-Macías, *Carbon* **2021**, *184*, 923.
[30] S. Jung, H. W. Choi, F. C. Mocanu, D.-W. Shin, M. F. Chowdhury, S. D. Han, Y.-H. Suh, Y. Cho, H. Lee, X. Fan, S. Y. Bang, S. Zhan, J. Yang, B. Hou, Y. T. Chun, S. Lee, L. G. Occhipinti, J. M. Kim, *Sci. Rep.* **2019**, *9*, 20376.
[31] M. F. Arif, S. Kumar, T. K. Gupta, K. M. Varadarajan, *Composites, Part A* **2018**, *113*, 141.
[32] F. Xue, Q. Peng, R. Ding, P. Li, X. Zhao, H. Zheng, L. Xu, Z. Tang, X. Zhang, X. He, *npj Flex. Electron.* **2024**, *8*, 14.
[33] M. Utzeri, M. Sasso, V. S. Deshpande, S. Kumar, *Adv. Mater. Technol.* **2024**, 2400457.
[34] S. Malek, L. Gibson, *Mech. Mater.* **2015**, *91*, 226.
[35] O. Kaynan, A. Yıldız, Y. E. Bozkurt, E. Ozden Yenigun, H. Cebeci, *Compos. Struct.* **2020**, *237*, 111930.
[36] S. Kumar, J. Ubaid, R. Abishera, A. Schiffer, V. S. Deshpande, *ACS Appl. Mater. Interfaces* **2019**, *11*, 42549.
[37] M. Sasso, G. Newaz, D. Amodio, *Mater. Sci. Eng., A* **2008**, *487*, 289.
[38] P. Grassl, D. Xenos, U. Nyström, R. Rempling, K. Gylltoft, *Int. J. Solids Struct.* **2013**, *50*, 3805.
[39] M. A. S. Matos, V. L. Tagarielli, P. M. Baiz-Villafranca, S. T. Pinho, *J. Mech. Phys. Solids* **2018**, *114*, 84.
[40] J. J. Ku-Herrera, F. Avilés, G. D. Seidel, *Smart Mater. Struct.* **2013**, *22*, 085003.
[41] W. Luheng, D. Tianhuai, W. Peng, *Carbon* **2009**, *47*, 3151.
[42] M. U. Azam, A. Schiffer, S. Kumar, *J. Mater. Res. Technol.* **2024**, *28*, 1359.
[43] J. Schneider, M. Ebert, R. Tipireddy, V. R. Krishnamurthy, E. Akleman, S. Kumar, *Addit. Manuf.* **2024**, *88*, 104213.
[44] J. Ubaid, J. Schneider, V. S. Deshpande, B. L. Wardle, S. Kumar, *Adv. Eng. Mater.* **2022**, *24*, 2200194.
[45] J. Schneider, M. Utzeri, K. Vinayak, A. Ergun, S. Kumar, (In review) **2024**.
[46] O. W. Saadi, M. A. Uddin, A. Schiffer, S. Kumar, *Adv. Eng. Mater.* **2023**, 2300473.
[47] J. J. Andrew, H. Alhashmi, A. Schiffer, S. Kumar, V. S. Deshpande, *Mater. Des.* **2021**, *208*, 109863.
[48] D. Xiang, X. Zhang, Y. Li, E. Harkin-Jones, Y. Zheng, L. Wang, C. Zhao, P. Wang, *Composites, Part B* **2019**, *176*, 107250.
[49] Z. Ma, A. Wei, J. Ma, L. Shao, H. Jiang, D. Dong, Z. Ji, Q. Wang, S. Kang, *Nanoscale* **2018**, *10*, 7116.
[50] W. Huang, K. Dai, Y. Zhai, H. Liu, P. Zhan, J. Gao, G. Zheng, C. Liu, C. Shen, *ACS Appl. Mater. Interfaces* **2017**, *9*, 42266.
[51] Y. Fei, F. Chen, W. Fang, L. Xu, S. Ruan, X. Liu, M. Zhong, T. Kuang, *Composites, Part B* **2020**, *199*, 108279.
[52] Y. Zhai, Y. Yu, K. Zhou, Z. Yun, W. Huang, H. Liu, Q. Xia, K. Dai, G. Zheng, C. Liu, C. Shen, *Chem. Eng. J.* **2020**, *382*, 122985.
[53] S. Xu, X. Li, G. Sui, R. Du, Q. Zhang, Q. Fu, *Chem. Eng. J.* **2020**, *381*, 122666.
[54] Z. Li, D. Feng, B. Li, D. Xie, Y. Mei, *Compos. Sci. Technol.* **2023**, *231*, 109803.
[55] F. J. Gibson, M. F. Ashby, *Cellular Solids: Structure and Properties*, Cambridge University Press, Cambridge **1997**, https://doi.org/10.1017/CBO9781139878326.